

Full length article

Meta-DNET-UPI: Efficient underwater polarization imaging combining deformable convolutional networks and *meta*-learning

Xueqiang Fan^a, Menglei Ding^b, Tianyi Lv^b, Xixun Sun^a, Bing Lin^a, Zhongyi Guo^{a,*}

^a School of Computer and Information, Hefei University of Technology, Hefei, 230009, China

^b 713th Research Institute, China State Shipbuilding Corporation Limited (CSSC), Zhengzhou, 450015, China

ARTICLE INFO

Keywords:

Underwater polarization imaging
Scattering medium
Polarization information processing
Deformable convolutional networks

ABSTRACT

Deep learning (DL) technology has demonstrated remarkable progress in solving the problem of underwater polarization imaging (UPI). However, most DL-based UPI methods heavily rely on large amount of labeled data, which is extremely time-consuming and cost-intensive. Furthermore, they cannot provide high-quality perception and simultaneously retrieve full geometry of objects. To address these limitations, we herein exploit the merit of *meta*-learning and propose a two-stage UPI computational method, Meta-DNET-UPI, based on *meta*-learning protocol with a deformable network, which achieves a higher UPI performance utilizing fewer training samples compared to state-of-the-art methods. Specifically, the development of Meta-DNET-UPI involves two stages: (i) we integrate deformable convolutional networks into U-Net (DNET) as base-learner for learning the transferable *meta*-knowledge of targets under different polarization characteristics' highly turbid underwater. More importantly, the DNET can capture the objects at various geometries and scales by adjusting the receptive fields adaptively in accordance to objects' scales and geometries. (ii) DNETs with multiple shared-parameters are fine-tuned on the *meta*-knowledge to learn the target task. Finally, to train our model, we establish an underwater optical scattering system and construct an underwater polarization scattering dataset, covering more abundant real-world scenarios. Extensive experiments demonstrate that the proposed method yields favorable image quality and rich visible details, and transcends other state-of-the-art methods in terms of visual quality and quantitative evaluation.

1. Introduction

Achieving high-quality imaging in turbid water is an essential but long-standing optical imaging problem. It enables a series of potential applications in various domains, ranging from remote sensing observation, marine resources detection, to underwater warfare, and underwater archaeology [1–5]. However, it remains an extremely challenging task due to several reasons: 1) In turbid water, suspending microparticles may absorb and scatter target signal, causing a dramatic degradation of imaging quality; 2) Light exhibits high sensitivity to microscopic-scale changes in the morphology of the target structure. Much effort has been made to cope with this challenge and some methods have been developed, such as optical coherence tomography, wavefront shaping, and transmission matrices [6–12]. Nevertheless, reconstructing underwater target information via these conventional optical experimental technologies is often laborious, costly, and time-consuming. Given the importance of underwater imaging and the difficulty in experimentally

retrieving target information, coupled with the urgent need for underwater imaging technology in various industries, there is now a growing interest in developing cost-effective computational methods for achieving high-performance underwater imaging.

To date, a series of methods have emerged for enhancing the underwater imaging quality [13–16], including visual prior-based methods (e.g., contrast-limited adaptive histogram equalization [17] and block-matching 3-D filtering (BM3D) [18]), physical model-based methods (e.g., dark channel prior (DCP) [19,20] and Retinex theory [21]), and polarization information-assisted methods [1,2,22]. Among them, the polarization imaging (PI) method exhibits its distinct advantages, owing to the fact that the difference of polarization characteristics between target signal and backscattered light [22–26]. These existing underwater polarization imaging (UPI) methods can be roughly grouped into the following two main categories according to the work modes: physical model-based and DL-based methods. In the early stage, physical model-based methods, such as polarization difference imaging, dominated in

* Corresponding author.

E-mail address: guozhongyi@hfut.edu.cn (Z. Guo).

the UPI field. These physical model-based methods generally focus on accurately estimating polarimetric measurements and parameters of interest [27]. Liang *et al.* [10] use three Stokes parameters, which are calculated from several images photographed by a polarizer in specific orientations, to realize the polarization image recovery. There is no denying that the physical model-based methods enable a well-informed interpretation of the intrinsic physical mechanisms of imaging through turbid water. However, physical model-based PI methods have a common drawback: they generally have apparent uncertainty as physical processes are highly complex, which severely limits application performance.

Compared to physical model-based methods, DL-based methods are not required to consider complex physical models since deep neural networks have powerful feature extraction and feature learning capabilities. During the last few years, a number of DL algorithms have been utilized to reconstruct polarization scattering images, and a series of DL-based methods have been developed, including Polarimetric-Net [28], AOD-Net [29], IPLNet [30], PDRDN [31], PFNet [32], U²R-pGAN [33], MU-DLU [34], and SAM-MIU-net [35], TIU-Net [36], etc [37–39]. These DL-based methods often utilize polarization scattering image information to recovery target information with one or more DL algorithms, such as convolutional neural networks (CNNs). For instance, in Polarimetric-Net, a dense connected neural network is employed to learn a UPI model on a large amount of polarization image dataset and the results show that the image restoration based on polarization information is superior to that based on intensity information alone. In MU-DLU, Li *et al.* [34] use the U-Net [40] to train the polarization scattering imaging model on a synthesized dataset generated by the Monte Carlo algorithm [41]. In recent work SAM-MIU-net, Lin *et al.* [35] integrate a self-attention module into the U-Net to extract multidimensional information from polarization speckle image, thereby enhancing polarization imaging further. Each of the aforementioned DL-based methods has its own advantage, and does play a role in stimulating the development of this important area. Meanwhile, they also have some disadvantages, as reflected by the following facts: 1) most DL-based UPI methods require an excessive amount of labeled data to construct the UPI model, which is extremely time-consuming and costly; 2) the performance of existing methods is awkward and poor generalizability in the face of real-world targets with various geometries and scales to be restored.

On the other hand, unlike some polarization-free underwater imaging approaches including DCP, GUDCP [20], WWPF [42], UWCNN [43], and SMDR-IS [44], we investigate the inability to recognize an object of interest in the strong scattering environment with the naked eye (see

[Fig. 1](#) for details), *i.e.*, the object stays in a state of “Hardly visible (in highly turbid water)”. Further, the focus of our approach is to use polarization information that provides multidimensional information beyond traditional intensity imaging to solve underwater optical scattering imaging problems.

The concept of *meta*-learning has undergone evolution over time, and it remains a vibrant domain of research in the field of machine learning [45]. The initial objective of the ML approach was to enhance algorithm performance through knowledge sharing across tasks and acquiring optimal strategies for applying existing learning algorithms to new ones. The emphasis has gradually shifted towards the development of models capable of rapid adaptation to novel tasks with limited data [46]. The training of a *meta*-learner typically involves two stages: *meta*-training and *meta*-testing. The model undergoes exposure to a diverse range of tasks during *meta*-training, aiming to acquire a comprehensive problem-solving strategy that can be effectively applied to novel tasks. The model undergoes *meta*-testing, where it is exposed to a novel task and leverages the acquired knowledge from *meta*-training to swiftly adapt and solve the new task.

In this work, we strive to confront challenges toward high-performance UPI in dense turbid water. The primary challenge toward this goal is to design a high-generalization scheme that is capable enough to learn the knowledge between polarization information and target radiance with a small number of polarization training samples. The second challenge is to design a module that can adaptively capture information about targets with different geometries and scales. Motivated by these ideas, herein, we propose a two-stage DL-based pipeline, called Meta-DNET-UPI, for high-performance UPI through turbid water. For the proposed Meta-DNET-UPI, three main contributions are made to enhance the performance of the UPI:

(i) Meta-DNET-UPI attempts to embed polarization characteristics in turbid water environments into *meta*-representation learning for UPI enhancement.

(ii) To achieve high-generalization performance with targets that vary in size, texture, and shape, we integrate deformable convolutional networks into the U-Net to capture the targets at various geometries and scales by adaptively adjusting the receptive fields while simultaneously extracting abundant context information through concatenating low-level feature maps and high-level ones.

(iii) Currently, owing to the extreme difficulty of acquiring polarization images in a scattering environment, there are no publicly available datasets. Thereby, we establish one scattering system under highly turbid water and construct an UPI dataset covering more abundant real-world scenes, which facilitates the further development of the UPI

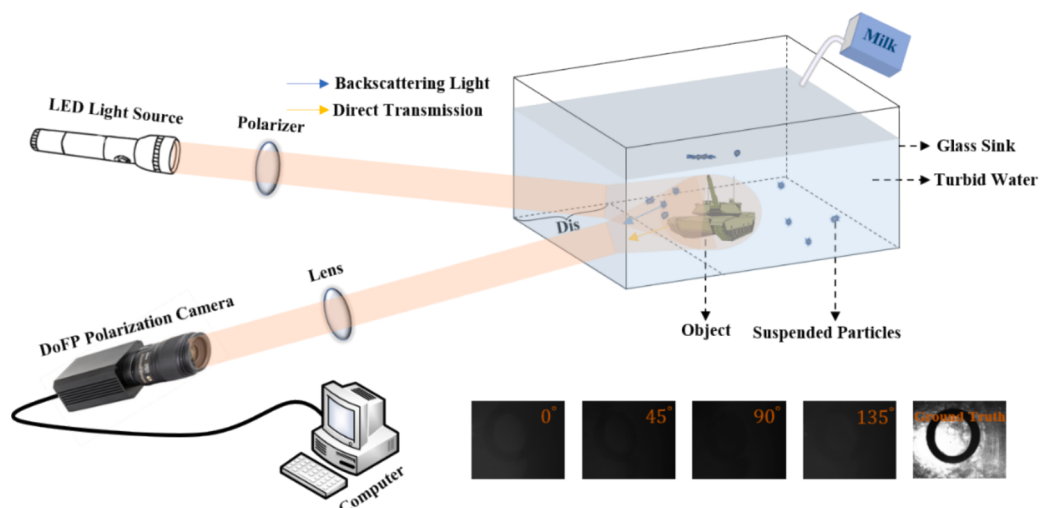


Fig. 1. Experimental setup for the polarization imaging through turbid underwater, and the obtained images $I_{0^\circ}(x, y)$, $I_{45^\circ}(x, y)$, $I_{90^\circ}(x, y)$, $I_{135^\circ}(x, y)$, and ground truth from the DoFP polarization camera.

techniques.

Finally, numerous experimental results indicate that our method achieves excellent performance in the UPI from the subjective and objective analysis, outperforming other advanced methods. Also, our method exhibits strong robustness across different testing datasets.

2. Method

2.1. Basic knowledge of underwater polarization imaging

In this work, inspired by the fact that backscattered light is partially polarized, polarization information is used to further enhance underwater image reconstruction quality. Meanwhile, we utilize Stokes parameters $S = [S_0(x, y), S_1(x, y), S_2(x, y), S_3(x, y)]^T$ to represent the polarization information. Each component in the Stokes parameters can be extracted from four polarization images, i.e., $I_{0^\circ}(x, y)$, $I_{45^\circ}(x, y)$, and $I_{90^\circ}(x, y)$, taken by orienting linear polarizer at 0° , 45° , 90° , and 135° in the same scene. Generally, circularly polarized light is rarely available in the natural environment, thus $S_3(x, y)$ component is ignored in this work. The Stokes parameters can be expressed as:

$$\begin{aligned} S_0(x, y) &= I_{0^\circ}(x, y) + I_{90^\circ}(x, y), \\ S_1(x, y) &= I_{0^\circ}(x, y) - I_{90^\circ}(x, y), \\ S_2(x, y) &= I_{45^\circ}(x, y) - I_{135^\circ}(x, y), \end{aligned} \quad (1)$$

where $S_0(x, y)$ refers to the total intensity received by the camera; $S_1(x, y)$ represents the intensity difference between the vertical and horizontal components; $S_2(x, y)$ denotes the intensity difference between the 45° and 135° components.

2.2. Measurement system

As shown in Fig. 1, we use a high permeability glass sink as a turbid media container, whose four surfaces are covered with black light-absorbing paper to avoid the effect of reflected light from the glass walls. The turbid water is utilized as the scattering medium. The light is focused by means of a convex lens. To make the taken images contain more obvious polarization information, a linear polarizer is employed as the polarization state generator to provide polarized illumination in front of the green LED light source. Different amounts of skimmed milk are injected into the glass sink filled with water to simulate the underwater environment with different scattering levels. Here, ‘Dis’ represents the distance between the objects and the water surface. We use a commercial division of focal plane (DoFP) polarization camera, whose spatial resolution is $2448 \times 2048 \times 3$, to take the polarization images containing the linear polarization information. Specifically, the surface of the DoFP polarization camera’s pixel array is covered with a polarization array consisting of micro-polarizers with four different polarization orientations of 0° , 45° , 90° , and 135° . Thus, for each single shot, DoFP polarization camera can photograph simultaneously four polarized images, i.e., $I_{0^\circ}(x, y)$, $I_{45^\circ}(x, y)$, $I_{90^\circ}(x, y)$, and $I_{135^\circ}(x, y)$. Using the digit made of steel as an example, Fig. 1 shows separately the $I_{0^\circ}(x, y)$, $I_{45^\circ}(x, y)$, $I_{90^\circ}(x, y)$, $I_{135^\circ}(x, y)$, and ground truth. Note that it is impossible to discern the targets in the scattering images by naked eyes. In this paper, I_{0° , I_{45° , S_0 , and S_1 , are selected as feature sources for the following reasons. We use the polarized illumination $S=(1, 1, 0, 0)^T$ to collect different polarization components. I_{0° component contains sufficient light intensity, whereas I_{90° component has relatively low light intensity. Additionally, I_{45° and I_{135° components may have similar illumination characteristics, which results in less valuable information for target detection from S_2 ($I_{45^\circ} - I_{135^\circ}$).

2.3. Pipeline of Meta-DNET-UPI

Deformable Convolutional Neural Network: a huge challenge in the UPI reconstruction is to model the targets with various geometries and

scales. Existing methods, such as common convolutions, extract target features through fixed receptive field, which may inevitably bring bias. As shown in Fig. 2, the deformable convolutional networks [47] (deformable-Conv) solve this problem by introducing deformable convolutional layers and deformable ROI pooling layers into the traditional neural networks. To be concrete, unlike traditional convolution, deformable-Conv incorporates learned offsets from previous feature maps generated by additional convolutional layers into the grid sampling locations. Thus, the deformable receptive field can effectively capture various geometries and scales that are adaptable to input features. Motivated by the idea of deformable-Conv, we integrate the deformation convolution into U-Net to enable it to adapt to different geometries, scales, etc.

Deformable Network (DNET): Recently deep learning techniques have started to emerge as an alternative way to optical computational imaging [48,49] including the UPI problems. Inspired by U-Net and deformable-Conv, we proposed a deformable network, called DENT, for the underwater polarization images (UPIs) recovery. Fig. 3 illustrates the network architecture. DENT is composed of four down-sampling layers (*Encoder*) that distill increasingly complex polarization information representations of the input, followed by four up-sampling layers (*Decoder*), with lateral connections from the *Encoder* to fill in contextual information. In each *Encoder* and *Decoder* stage, DENT employs deformable-Conv blocks to model targets of various shapes and scales through learning local, dense and adaptive receptive fields. Each deformable convolutional block comprises a convolution offset layer with kernel size 3×3 , a convolution layer with kernel size 3×3 , a batch normalization layer, and an ReLU activation layer. During the *Decoder* stage, DENT also inserts a common convolution layer after the merge operation to adjust the filter numbers for the convolution offset layer. This architecture enables DENT to learn discriminative features and produce detailed information about target’s polarization characteristics.

Meta-Learning based Underwater Polarization Imaging Pipeline: To tackle the significant issue that most methods for building models rely on a large number of training samples, a novel the UPIS reconstruction approach is proposed, named Meta-DNET-UPI. Meta-DNET-UPI is based on *meta*-learning techniques [45,50], also known as learning-to-learn, which aim to enable data-driven models to learn how to learn given only a small amount data. In *meta*-learning, a model is trained with different tasks and then used to rapidly learn new tasks [50]. Following the core idea of *meta*-learning, our proposed Meta-DNET-UPI consists of two stages, namely, *meta*-representation learning and target-task learning, and its pipeline can be seen in Fig. 4. To be more precise, in the first phase, the proposed DNET is chosen as base-learner. It tries to learn how to represent polarization characteristics of target’s three different polarization state (i.e., $I_{0^\circ}(x, y)$, $I_{45^\circ}(x, y)$, and $S_1(x, y)$):

$$\begin{aligned} \widetilde{I}_{0^\circ}(x, y) &= DNET_0(I_{0^\circ}(x, y), w_\Phi), \\ \widetilde{I}_{45^\circ}(x, y) &= DNET_1(I_{45^\circ}(x, y), w_\Psi), \\ \widetilde{S}_1(x, y) &= DNET_2(S_1(x, y), w_\Omega), \end{aligned} \quad (2)$$

where w_Φ , w_Ψ , and w_Ω represent respectively the transferable *meta*-knowledge of target’s $I_{0^\circ}(x, y)$, $I_{45^\circ}(x, y)$, and $S_1(x, y)$ in highly turbid underwater learned by the base-learners (i.e., $DNET_0$, $DNET_1$, and $DNET_2$); $\widetilde{I}_{0^\circ}(x, y)$, $\widetilde{I}_{45^\circ}(x, y)$, and $\widetilde{S}_1(x, y)$ represent objective function of different tasks. Note that, the parameters of base-learners containing network’s parameters and the number of base-learners are tuned during the *meta*-train stage and stay fixed after each task learning. During the target-task learning phase, DNETs with multi shared-parameters based on the prior knowledge are adopted to fine-tune the mapping between the target radiance and the *meta*-knowledge: $T_{\text{target}} = DNET(DNET(DNET(S_0(x, y), w_Y), w_Y), w_Y)$, where T_{target} is final reconstruction image; w_Y is the parameter learned by the base-learner.

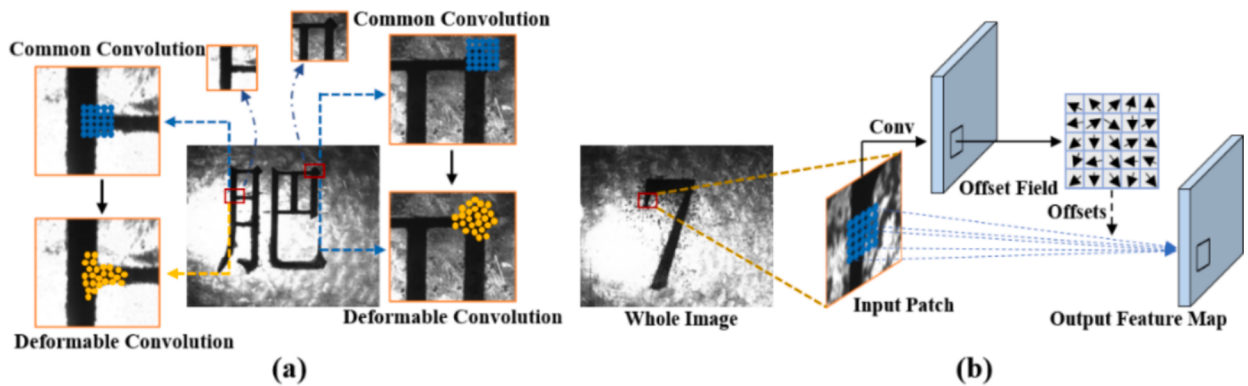


Fig. 2. (a) Experimental setup for the PSI through scattering medium, (b) The obtained images ($I_{0^\circ}(x, y)$, $I_{45^\circ}(x, y)$, $I_{100^\circ}(x, y)$, and $I_{135^\circ}(x, y)$) from the DoFP polarization Camera, the calculated DoLP image, and the ground truth.

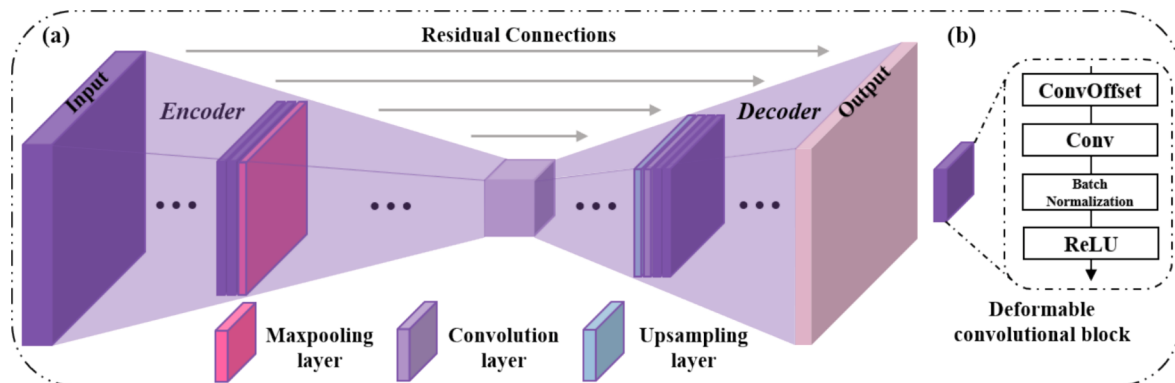


Fig. 3. (a) Illustration of Deformable Network. Its architecture with convolutional encoder and decoder using (b) deformable convolutional block based on U-Net architecture.

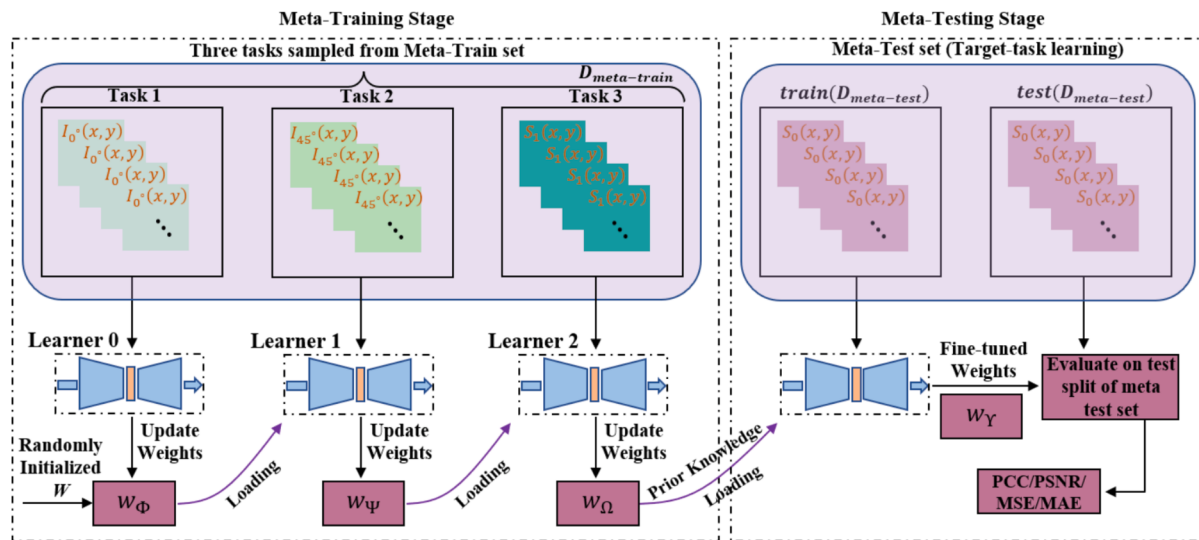


Fig. 4. Pipeline of Meta-DNET-UPI. (a) Meta-train stage. (b) Target-task learning.

2.4. Training details and evaluation metrics

Meta-DNET-UPI and all the comparison methods are implemented in the PyTorch deep learning framework [51]. Considering the limitations of GPU capacity, all images are adjusted into a fixed size, i.e., 256×256 . In the training procedure, data augmentation strategies based on Scikit-image Python library [52] are used for all the methods, including

random horizontal and vertical flipping. The initial learning rate is set to $2e^{-4}$ and divided by 10 after every 10 epochs, and the maximum number of training epochs is set to 150. We adopt the Adam algorithm as the optimizer to optimize the model parameters. All experiments are performed on Linux Server Intel (R) Core (TM) i7-7700 CPU @3.6 Hz 48.0 GB of RAM, and Python 3.7 programming. To speed up training, the models are trained on a single Nvidia GeForce RTX 3090 GPU with the

mean square error loss \mathcal{L}_{mse} .

Four commonly used image quality metrics, i.e., Pearson Correlation Coefficient (PCC), Mean Square Error (MSE), Peak Signal-to-Noise Ratio (PSNR), and Mean Absolute Error (MAE), are selected to evaluate the quality of image recovery. We use the PCC to quantify the relationship between the recovered and true pixel-level values for each image, with values between -1 and 1 . MSE is applied to quantitatively measure the average deviation between the reconstructed and ground truth pixel-level values of each image. In addition, we also use PSNR to quantify the content between the reconstructed and real images, with higher PSNR values representing closer image content. MAE is utilized to quantitatively measure the average absolute deviation between the reconstructed and ground truth pixel-level values of each image. The larger the PCC and PSNR, the more favorable the outcome, whereas the opposite holds true for MSE and MAE.

3. Result and discussion

3.1. Benchmark dataset

To train our proposed model, in this work, a new benchmark dataset is constructed by using self-constructed experimental setup. To be specific, first, the glass sink is filled with water, and the object of interest is placed inside at a depth of Dis cm from the water surface. Meanwhile, the DoFP polarization camera is placed away from the glass sink to produce ground truth images. Then, we blend the water with skimmed milk to make it turbid and activate the camera to obtain the scattering image of the object. Finally, we experimentally build one training dataset, which is composed of 100 groups polarization images. Each group has eight images corresponding to $I_{0^\circ}(x, y)$, $I_{45^\circ}(x, y)$, $S_0(x, y)$, $S_1(x, y)$, as well as their corresponding ground truths. Let $D = \{D_1, \dots, D_i, \dots, D_n\}_{i=1}^4$ represents total of four datasets and each dataset is defined as $D_i = \{(x, y)_j\}_{j=1}^k$, where $(x, y)_j$ denotes a pair of images and its corresponding label; K is total number of samples. Thereafter, D is split into *meta-train* set ($D_{meta-train}$), which encompasses images of three different polarization state and remaining set is *meta-test* set ($D_{meta-test}$) for target-task learning. Note that, each sample in the training dataset is generated under such conditions that the water surface-to-object distance Dis and the turbidity are set to 9 cm and 133.3NTU, respectively, and the targets are only a variety of simple digits. Finally, 80 groups of images in dataset are as the training set and the remains as validation dataset.

The optical thickness of the medium can be as a measure of its scattering capability and is proportional to the scattering medium coefficient and the distance between the camera and the object [53]. In other words, by adding different volumes of milk or adjusting the distance of the camera from the target, it is equivalent to changing the turbidity of the scattering medium. Hence, in the next experiments, we explore the generalization performance of our proposed method by varying the parameters Dis and NTU (refer to Section ‘**Evaluating the Performance of Our Proposed Meta-DNET-UPI**’ for details). In addition, we also investigate the effect of the objects’ geometry and its constituent materials on the performance of the proposed method. Collectively, we collect four testing datasets, named GEO, DIS, ONTU (objects at different underwater turbidities), and MAT, respectively. It should be noted that there are no publicly available datasets due to the extreme difficulty of obtaining polarization images in a scattering environment.

3.2. Ablation experiments

(1) **Performance Comparisons between U-shaped network based on normal convolution (abbreviated as Normal-U-Net for convenience) and U-shaped network based on deformable convolution**

(abbreviated as Deformable-U-Net for convenience).

This section examines to what extent the introduced deformable-Conv can help to reconstruct the UPIS, especially with respect to target details. Specifically, two separate network structures, i.e., Normal-U-Net and Deformable-U-Net, will be investigated. We testify the performance of restoring the UPIS on both network structures over the independent validation tests on the training dataset and validation dataset. Fig. 5 shows their visual comparison results, and detailed results are listed in Table 1.

From Fig. 5 and Table 1, it is easy to see that Deformable-U-Net consistently outperforms Normal-U-Net concerning the four evaluation indexes. Concretely, the PCC, PSNR, MAE, and MSE are 0.78, 13.86, 0.15, and 0.046, which are 2.63 %, 10.26 %, 11.76 %, and 20.68 %, higher than those of Normal-U-Net, respectively. Furthermore, from the perspective of visual quality, the significant visible details gain by Deformable-U-Net indicates that it is valid to use deformable convolution to optimize our model.

(2) **Meta-Learning is better than Direct Learning.** In this section, we perform experiments to research the performance of our DNET with different training strategies, i.e., *meta*-learning and direct learning, on the training dataset. Here, ‘Direct Learning’ means that only a single model (i.e., DNET) is trained to reconstruct the UPIS. The architecture of our proposed Meta-DNET-UPI model based on *meta*-learning is shown in Fig. 4. The comparison results are presented in Table 1 and Fig. 5.

From Table 1, it is straightforward to find that *meta*-learning-based Meta-DNET-UPI model overall outperforms direct learning. For example, the average PCC value of Meta-DNET-UPI is 0.81, which is 3.85 % higher than the average of direct learning, respectively. Notably, as listed in Fig. 5, our Meta-DNET-UPI yields the UPIS reconstruction more effectively while retrieving the fine image details. The above comparison results can demonstrate that the performance is indeed enhanced after applying *meta*-learning scheme.

3.3. Evaluating the performance of our Meta-DNET-UPI

To ensure the reasonability of the experiments, during this section, we perform imaging experiments to verify the effectiveness of the proposed Meta-DNET-UPI. Specifically, we design four scenarios for evaluating the performance of our Meta-DNET-UPI. In order to assess the performance of our method in a comprehensive, stable and fair manner, we evaluate the effectiveness of our method on each test dataset.

(1) **Evaluation on Underwater Targets of Different Geometries.** We collect one testing dataset to validate the performance of Meta-DNET-UPI owing to the change in targets with different geometries. It contains 24 samples. Each sample in the testing dataset is produced in the same underwater environment as the samples in the training dataset, i.e., the water surface-to-object distance $Dis = 9$ cm and the turbidity $NTU = 133.3$. It should be noted that, unlike the geometry of the targets in the training set, the geometry of the targets in this testing dataset includes three categories, i.e., untrained digits, letters, and Chinese characters. Table 2 and Figs. 6, 7, and 8 display the performance of

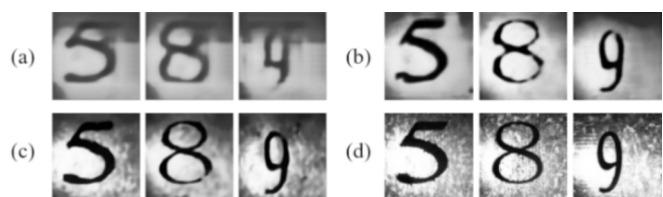


Fig. 5. (a) and (b) comparison highlights that deformable-Conv can enhance the performance of reconstructed underwater polarization images in target details. (b) and (c) comparison highlights that *meta*-learning is better than direct learning. (a), (b), and (c) are the images recovered by Normal-U-Net, Deformable-U-Net, and Deformable-U-Net with *meta*-learning, respectively. (d) Ground truths.

Table 1

Performance comparison of different network architectures. $\uparrow\downarrow$ denote larger and smaller is better, respectively.

| Network | PCC \uparrow | PSNR \uparrow | MAE \downarrow | MSE \downarrow |
|-------------------------------------|----------------|-----------------|------------------|------------------|
| Normal-U-Net | 0.76 | 12.57 | 0.17 | 0.058 |
| Deformable-U-Net | 0.78 | 13.86 | 0.15 | 0.046 |
| Deformable-U-Net with meta-learning | 0.81 | 14.19 | 0.14 | 0.043 |

Table 2

Performance demonstrations of Meta-DNET-UPI on the underwater targets of different geometries.

| Target | PCC \uparrow | PSNR \uparrow | MAE \downarrow | MSE \downarrow |
|-------------------|----------------|-----------------|------------------|------------------|
| Digital | 0.83 | 14.49 | 0.14 | 0.038 |
| Letter | 0.83 | 14.14 | 0.15 | 0.039 |
| Chinese Character | 0.81 | 14.24 | 0.15 | 0.039 |

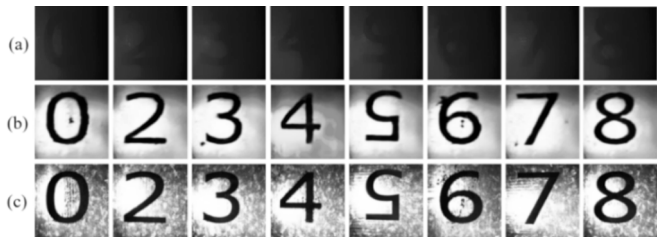


Fig. 6. Visual demonstrations of our Meta-DNET-UPI reconstruction on untrained digit targets. (a) The scattering image $I_0^o(x, y)$. (b) The images recovered by our Meta-DNET-UPI. (c) Ground truths.



Fig. 7. Visual demonstrations of our Meta-DNET-UPI reconstruction on untrained letter targets. (a) The scattering image $I_0^o(x, y)$. (b) The images recovered by our Meta-DNET-UPI. (c) Ground truths.

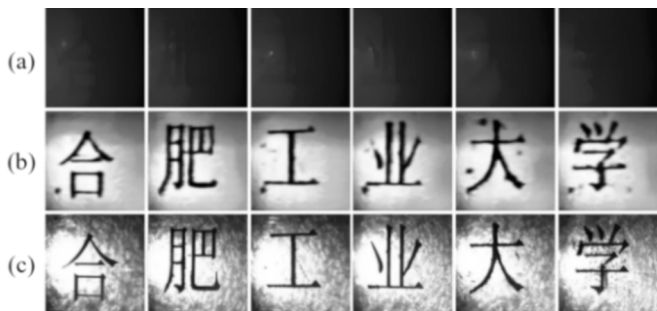


Fig. 8. Visual demonstrations of our Meta-DNET-UPI reconstruction on untrained Chinese characters. (a) The scattering image $I_0^o(x, y)$. (b) The images recovered by our Meta-DNET-UPI. (c) Ground truths.

Meta-DNET-UPI concerning quantitative evaluation and visual quality, respectively.

It is apparent from Table 2 that Meta-DNET-UPI achieves superior reconstruction results on three classes of untrained geometric targets

concerning the four evaluation indexes. Concretely, Meta-DNET-UPI reaches $\text{PCC} > 0.81$, $\text{PSNR} > 14.14$, $\text{MAE} > 0.14$, and $\text{MSE} > 0.038$ on the three classes of untrained geometric targets. Additionally, according to the average PCC and PSNR of the Meta-DNET-UPI for the three types of untrained targets, we can find that Meta-DNET-UPI yields the best performance for the untrained digit targets, followed by letter targets and Chinese character. As can be seen from Figs. 6, 7, and 8, well-defined visual details and high-quality geometric shapes can be observed in the restored images of Meta-DNET-UPI, which correspond closely to ground truths.

(2) **Evaluation on Targets of Different Underwater Imaging Distances.** Herein, we perform experiments to investigate the influences of different imaging distances, *i.e.*, the water surface-to-object distance Dis , on the performance of our Meta-DNET-UPI. We design and conduct a sequence of independent test on one testing dataset. It consists of five groups, which are produced under the conditions where the distance (Dis) from the water surface to the object is changed to 8 cm, 9 cm, 10 cm, 12 cm, and 13 cm, while simultaneously ensuring the turbidity NTU is set to 133.3. It has 40 samples. A comparison of recovery performance of our Meta-DNET-UPI for various underwater imaging distances is provided in Table 3. Fig. 7 illustrates a visual comparison of recovery results of our Meta-DNET-UPI.

As described in Table 3, it is clear that the reconstruction performance of the Meta-DNET-UPI at $Dis = 9$ cm is superior to those at $Dis = 8$ cm, $Dis = 10$ cm, $Dis = 12$ cm, and $Dis = 13$ cm in terms of all four evaluation indexes. Specifically, compared with $Dis = 8$ cm, the second-best performance's distance from the viewpoint of PCC and PSNR, the PCC and PSNR of Meta-DNET-UPI at $Dis = 9$ cm are 0.78 and 13.75, which are 1.30 % and 2.38 %, respectively, higher than those at $Dis = 8$ cm. Furthermore, Fig. 9 shows that when $Dis = 8$ cm, 9 cm, and 10 cm, the images recovered by the Meta-DNET-UPI have well visual quality. When distance greater than 12 cm, although the performance of the Meta-DNET-UPI drops slowly in recovering image details, the background and target of the reconstructed image can be effectively distinguished.

(3) **Evaluation on Targets at Different Underwater Turbidity Levels.** To test whether Meta-DNET-UPI truly ‘learned’ the polarization characteristics that determine the quality of the reconstructed UPI, or is simply ‘remembers’ pairwise mapping between scattered images and ground truths, we look at the recovery performance of Meta-DNET-UPI on targets at different underwater turbidity levels. Hereby, a new testing dataset is collected, which consists of six underwater turbidity levels. Its samples are generated under the conditions that the turbidity NTU is changed to 119.8, 133.3, 148.3, 162.1, 174.3, and 187.1, respectively, while simultaneously securing the water surface-to-object distance Dis set to 9 cm. It consists of 144 samples. It is worth noting that as the value of NTU increases, the scattering coefficient becomes higher, in which case the polarization information of the object is further degraded.

By carefully observing Fig. 10 and Table 4, the following three phenomena can be seen: (i) Not surprisingly, the generalization capability of Meta-DNET-UPI at 133.3NTU is comparable to those at 119.8NTU, and outperforms those at 148.3NTU, 162.1NTU, 174.3NTU, and 187.1NTU with respect to four evaluation indexes. (ii) It is straightforward to find that the image recovered by the Meta-DNET-UPI have well structural integrity, when $NTU \leq 162.1$. While $NTU > 162.1$,

Table 3

Performance demonstrations of Meta-DNET-UPI on the targets of different underwater imaging distances.

| Distance | PCC \uparrow | PSNR \uparrow | MAE \downarrow | MSE \downarrow |
|----------|----------------|-----------------|------------------|------------------|
| 8 cm | 0.77 | 13.43 | 0.15 | 0.056 |
| 9 cm | 0.78 | 13.75 | 0.14 | 0.047 |
| 10 cm | 0.75 | 13.02 | 0.15 | 0.051 |
| 12 cm | 0.53 | 10.91 | 0.22 | 0.10 |
| 13 cm | 0.38 | 9.81 | 0.27 | 0.12 |



Fig. 9. Visual demonstrations of our Meta-DNET-UPI reconstruction on targets of different underwater imaging distances. (a) 8 cm. (b) 9 cm. (c) 10 cm. (d) 12 cm. (e) 13 cm.



Fig. 10. Visual demonstrations of our Meta-DNET-UPI reconstruction on targets at different underwater turbidity levels. (a) 119.8NTU. (b) 133.3NTU. (c) 148.3NTU. (d) 162.1NTU. (e) 174.3NTU. (f) 187.1NTU.

Table 4

Performance demonstrations of Meta-DNET-UPI on the targets of at different underwater turbidity levels.

| Turbidity (NTU) | PCC↑ | PSNR↑ | MAE↓ | MSE↓ |
|-----------------|------|-------|------|-------|
| 119.8 | 0.82 | 14.74 | 0.13 | 0.036 |
| 133.3 | 0.82 | 14.28 | 0.15 | 0.038 |
| 148.3 | 0.76 | 13.94 | 0.15 | 0.046 |
| 162.1 | 0.71 | 13.31 | 0.16 | 0.055 |
| 174.3 | 0.68 | 12.73 | 0.17 | 0.061 |
| 187.1 | 0.60 | 11.92 | 0.19 | 0.076 |

the target of the reconstructed image can be recognized, although the performance of the Meta-DNET-UPI is declined in recovering image details. (iii) It has not escaped our notice that our proposed Meta-DNET-UPI enjoys reconstructing underwater image under adverse conditions of high turbidity water, *i.e.*, NTU = 162.1, and the underwater turbidity level's generalization reaches to 20 % that can be an index for demonstrating excellence of our proposed Meta-DNET-UPI. These experimental results demonstrate that our Meta-DNET-UPI is robust and effective in reasonably dense turbid underwater environments.

(4) **Evaluation on Underwater Targets with Different Materials.** The polarization characteristics of the image signal are heavily influenced by the composition of the target material. To further evaluate the efficacy of proposed Meta-DNET-UPI, its generalization performance is also experimentally evaluated on a new testing dataset containing two types untrained targets with different materials, *i.e.*, Paper-Steel and Steel-Wood. The Paper-Steel and Steel-Wood mean digits (or letters) made of paper against steel background and digits (or letters) made of steel against wood background, respectively. It contains 10 samples. Table 5 and Fig. 11 list the quantitative and visual comparisons,

Table 5

Performance demonstrations of Meta-DNET-UPI on the underwater targets with different materials.

| Material | PCC↑ | PSNR↑ | MAE↓ | MSE↓ |
|-------------|------|-------|------|-------|
| Steel-Wood | 0.67 | 12.15 | 0.20 | 0.078 |
| Paper-Steel | 0.41 | 8.34 | 0.34 | 0.190 |



Fig. 11. Visual demonstrations of our Meta-DNET-UPI reconstruction on underwater targets with different materials. The first four columns are Paper-Steel, and the last four columns are Steel-Wood.

respectively. According to the PCC, PSNR, MAE, and MSE listed in Table 5, we can find that our proposed Meta-DNET-UPI shows the best performance on the Steel-Wood, followed by Paper-Steel. Concretely, among the two groups, Meta-DNET-UPI has the highest values of PCC, PSNR, MAE, and MSE on the Steel-Wood, reaching 0.67, 12.15, 0.20, and 0.078, respectively. It can be observed from Fig. 11 that the Meta-DNET-UPI can effectively distinguish the target and background. Moreover, despite the PCC and PSNR of Meta-DNET-UPI are 0.41 and 8.34 on the Paper-Steel, respectively, the structural outline of the target can be reconstructed well.

3.4. Comparison with state-of-the-art methods

This purpose of this section is to further experimentally demonstrate the efficacy of our proposed Meta-DNET-UPI by comparing it with other recently state-of-the-art UPI methods, including traditional methods, such as DCP [19], UDCP [54], BM3D [18], and CLAHE [17], as well as DL-based methods, such as MSBDN [55], Polarimetric-Net [28], MU-DLU [34], UWCNN [43], SAM-MIU-net [35], SMDR-IS [44] and TIU-Net [36]. For a fair comparison, all DL-based methods are trained on the same training dataset and evaluated on the same testing samples. Table 6 and Fig. 12 summarize the comparison results.

As can be seen from Table 6, it is apparent that the restoration performance of our Meta-DNET-UPI is superior to that of other methods. Specifically, compared with the SMDR-IS, Meta-DNET-UPI enjoys the improvements of 6.49 %, 7.02 %, 17.65 %, and 24.00 %, on PCC, PSNR, MAE, MSE, respectively. Meanwhile, Meta-DNET-UPI has achieved comparable performance to recent work TIU-Net. As expected, four non-DL-based methods, *i.e.*, DCP, UDCP, BM3D, and CLAHE, gain lower

Table 6

Performance comparison between Meta-DNET-UPI and other methods.

| Method | PCC↑ | PSNR↑ | MAE↓ | MSE↓ |
|------------------|------|-------|------|-------|
| DCP | 0.31 | 4.53 | 0.35 | 0.31 |
| UDCP | 0.27 | 3.73 | 0.55 | 0.41 |
| BM3D | 0.29 | 6.29 | 0.37 | 0.19 |
| CLAHE | 0.38 | 7.48 | 0.35 | 0.17 |
| MSBDN | 0.44 | 8.05 | 0.33 | 0.16 |
| Polarimetric-Net | 0.43 | 7.91 | 0.34 | 0.16 |
| MU-DLN | 0.72 | 11.15 | 0.22 | 0.064 |
| UWCNN | 0.75 | 13.22 | 0.18 | 0.051 |
| SAM-MIU-net | 0.74 | 11.71 | 0.20 | 0.062 |
| SMDR-IS | 0.77 | 13.25 | 0.17 | 0.050 |
| TIU-Net | 0.83 | 14.10 | 0.14 | 0.039 |
| Meta-DNET-UPI | 0.82 | 14.18 | 0.14 | 0.038 |

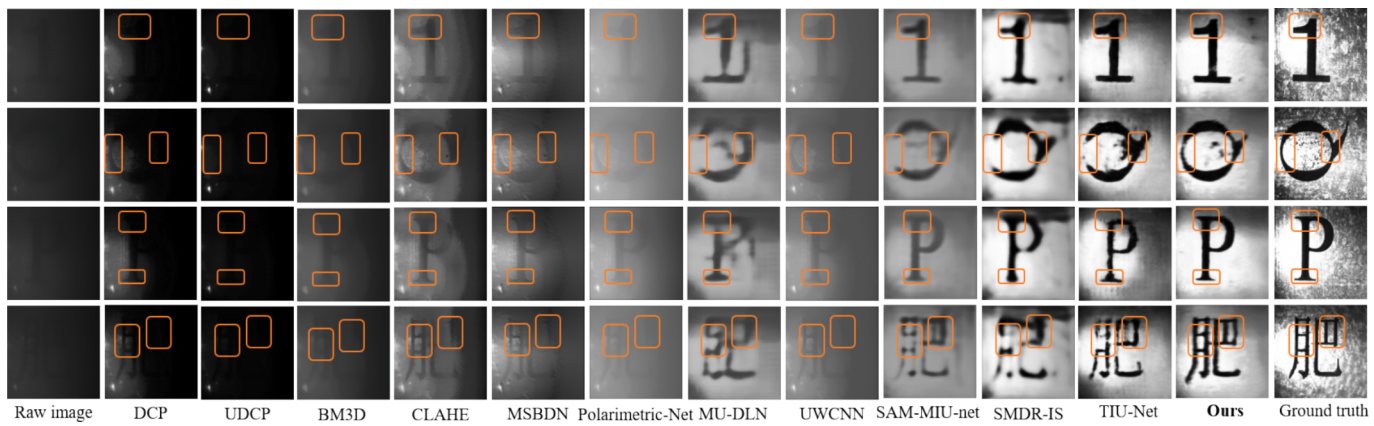


Fig. 12. Visual comparisons for underwater polarization image reconstruction between our method and state-of-the-art methods.

performance. On the other hand, Fig. 12 displays visual comparisons for the UPIS reconstruction between our method and state-of-the-art methods. Compared to the other approaches, our Meta-DNET-UPI more effectively achieves the UPIS reconstruction while preserving the fine image details. Clearly, taking the reconstruction results of Chinese character ‘肥’ as an example, our Meta-DNET-UPI delivers a more faithful representation of the target. As evidenced by the quantitative results in Table 6 and visual comparisons in Fig. 12, an interesting observation emerges: while TIU-Net demonstrates marginally superior performance in certain quantitative metrics, our proposed method achieves significantly better visual quality in object reconstruction tasks. The primary reason for this phenomenon is that TIU-Net places more emphasis on background reconstruction. In contrast, it inadequately meets the crucial requirement for accurate target reconstruction, which is the fundamental objective of this task. Therefore, we will consider integrating the two methods to further improve the quality of underwater imaging in future, and at the same time develop effective underwater evaluation indicators to mitigate this problem [56,57].

4. Conclusion

In this work, by leveraging the *meta*-learning and multi-dimensional characteristics of polarization information, we propose a novel method, named Meta-DNET-UPI, to realize high-performance UPIS. Experimental results demonstrate that the proposed Meta-DNET-UPI significantly outperforms other existing UPIS methods. The superior performance of Meta-DNET-UPI can be attributed to several factors, including careful construction of the model based on *meta*-learning philosophy, the subtle use of a deformable network, and an appropriate benchmark dataset. There are some limitations to our approach. For instance, in the dataset, the samples prepared so far are relatively simple due to the limitations of the experimental conditions. In the methodology, our approach lacks interpretability. The inner workings of the DL model are a black box to us, and we can obtain more if we can understand the underlying workings. The performance of DL-based computational imaging methods is optimal for high-contrast targets, but these methods are likely to encounter limitations when applied to complex scenes. In the future study, to further improve the performance of UPIS, we will concentrate on the following points: (1) designing a more accurate method by combining Meta-DNET-UPI and various macroscopically identical microscopically different scattering media; (2) exploring the relationship between 2D CNNs and 3D CNNs to fully mine discriminative information; (3) employing the suitable deep learning algorithm to obtain the available information extracted from the original scattering image representation; (4) developing effective evaluation metrics to evaluate the reconstructed object and background separately. Lastly, while much improvement has been achieved by our proposed Meta-DNET-UPI, further research on UPIS yet is an open question.

CRediT authorship contribution statement

Xueqiang Fan: Writing – original draft, Visualization, Software, Methodology, Investigation, Formal analysis, Data curation, Conceptualization. **Menglei Ding:** Resources, Methodology, Investigation, Formal analysis. **Tianyi Lv:** Resources, Methodology, Investigation, Formal analysis. **Xixun Sun:** Methodology, Investigation, Formal analysis, Data curation. **Bing Lin:** Investigation, Data curation. **Zhongyi Guo:** Writing – review & editing, Supervision, Project administration, Methodology, Funding acquisition, Formal analysis, Conceptualization.

Declaration of competing interest

The authors declare that they have no known competing financial interests or personal relationships that could have appeared to influence the work reported in this paper.

Acknowledgments

This research is funded by the National Natural Science Foundation of China under Grant 61775050. The computation of this research is supported by the HPC Platform of Hefei University of Technology.

Data availability

Data will be made available on request.

References

- [1] H.B. de Aguiar, S. Gigan, S. Brasselet, Polarization recovery through scattering media, *Sci. Adv.* 3 (9) (2017) e1600743.
- [2] S.B. Powell, R. Garnett, J. Marshall, et al., Bioinspired polarization vision enables underwater geolocation, *Sci. Adv.* 4(4):eaao6841 (2018).
- [3] S. Yoon, M. Kim, M. Jang, et al., Deep optical imaging within complex scattering media, *Nat. Rev. Phys.* 2 (3) (2020) 141–158.
- [4] H. Liu, X. Li, Z. Cheng, et al., Polarization Maintaining 3-D Convolutional Neural Network for Color Polarimetric Images Denoising, *IEEE Trans. Instrum. Meas.* 72 (2023) 1–9.
- [5] J. Xie, J. Dou, L. Zhong, et al., A Dual-Mode Intensity and Polarized Imaging System for Assisting Autonomous Driving, *IEEE Trans. Instrum. Meas.* 73 (2024) 1–13.
- [6] D. Huang, E.A. Swanson, C.P. Lin, et al., Optical Coherence Tomography. *Science* 254 (5035) (1991) 1178–1181.
- [7] A.P. Mosk, A. Lagendijk, G. Lerosey, et al., Controlling waves in space and time for imaging and focusing in complex media, *Nat. Photonics* 6 (5) (2012) 283–292.
- [8] J. Yoon, K. Lee, J. Park, et al., Measuring optical transmission matrices by wavefront shaping, *Opt. Express* 23 (8) (2015) 10158–10167.
- [9] X. Wang, T. Hu, D. Li, et al., Performances of polarization-retrieve imaging in stratified dispersion media, *Remote Sens.* 12 (18) (2020) 2895.
- [10] J. Liang, L. Ren, E. Qu, et al., Method for enhancing visibility of hazy images based on polarimetric imaging, *Photonics Res.* 2 (1) (2014) 38–44.
- [11] L. Valzania, S. Gigan, Online learning of the transmission matrix of dynamic scattering media, *Optica* 10 (6) (2023) 708–716.

- [12] X. Pu, X. Wang, X. Gao, et al., Sky Polarization Pattern Reconstruction and Neutral Line Detection Based on Adversarial Learning, *IEEE Trans. Instrum. Meas.*, 2023.
- [13] J. Zhou, Y. Wang, C. Li, et al., Multicolor light attenuation modeling for underwater image restoration, *IEEE J. Oceanic Eng.*, 2023.
- [14] X. Fan, B. Lin, K. Guo, et al., TSMPN-PSI: high-performance polarization scattering imaging based on three-stage multi-pipeline networks, *Opt. Express* 31 (23) (2023) 38097–38113.
- [15] J. Zhou, L. Pang, D. Zhang, et al., Underwater image enhancement method via multi-interval subhistogram perspective equalization, *IEEE J. Oceanic Eng.*, 2023.
- [16] J. Liang, L. Ren, R. Liang, Low-pass filtering based polarimetric dehazing method for dense haze removal, *Opt. Express* 29 (18) (2021) 28178–28189.
- [17] A.M. Reza, Realization of the contrast limited adaptive histogram equalization (CLAHE) for real-time image enhancement, *Journal of VLSI Signal Processing Systems for Signal, Image and Video Technology* 38 (2004) 35–44.
- [18] A. Abubakar, X. Zhao, S. Li, et al., A block-matching and 3-D filtering algorithm for Gaussian noise in DoFP polarization images, *IEEE Sens. J.* 18 (18) (2018) 7429–7435.
- [19] K. He, J. Sun, X. Tang, Single image haze removal using dark channel prior, *IEEE Trans. Pattern Anal. Mach. Intell.* 33 (12) (2010) 2341–2353.
- [20] Z. Liang, X. Ding, Y. Wang, et al., GUDCP: Generalization of underwater dark channel prior for underwater image restoration, *IEEE Trans. Circuits Syst. Video Technol.* 32 (7) (2021) 4879–4884.
- [21] E.H. Land, J.J. McCann, Lightness and retinex theory, *Josa* 61 (1) (1971) 1–11.
- [22] J. Liang, L. Ren, H. Ju, et al., Polarimetric dehazing method for dense haze removal based on distribution analysis of angle of polarization, *Opt. Express* 23 (20) (2015) 26146–26157.
- [23] T. Treibitz, Y.Y. Schechner, Active polarization descattering, *IEEE Trans. Pattern Anal. Mach. Intell.* 31 (3) (2008) 385–399.
- [24] Y.Y. Schechner, N. Karpel, Recovery of underwater visibility and structure by polarization analysis, *IEEE J. Oceanic Eng.* 30 (3) (2005) 570–587.
- [25] J. Liang, Y. Sun, L. Ren, et al., Short-wave infrared polarimetric image reconstruction using a deep convolutional neural network based on a high-frequency correlation, *Appl. Opt.* 61 (24) (2022) 7163–7172.
- [26] X. Fan, B. Lin, Z. Guo, Infrared Polarization-Empowered Full-Time Road Detection via Lightweight Multi-Pathway Collaborative 2D/3D Convolutional Networks, *IEEE Trans. Intell. Transp. Syst.* 25 (9) (2024) 12762–12775.
- [27] W.-Y. Chen, M. O'Toole, A.C. Sankaranarayanan, et al., Enhancing speckle statistics for imaging inside scattering media, *Optica* 9 (12) (2022) 1408–1416.
- [28] H. Hu, Y. Zhang, X. Li, et al., Polarimetric underwater image recovery via deep learning, *Opt. Lasers Eng.* 133 (2020) 106152.
- [29] Xiang Y, Ren Q, Chen R-P, A neural network for underwater polarization dehazing imaging, *Optoelectronic Imaging and Multimedia Technology VIII*, SPIE2021, pp. 1189702.
- [30] H. Hu, Y. Lin, X. Li, et al., IPLNet: a neural network for intensity-polarization imaging in low light, *Opt. Lett.* 45 (22) (2020) 6162–6165.
- [31] X. Li, H. Li, Y. Lin, et al., Learning-based denoising for polarimetric images, *Opt. Express* 28 (11) (2020) 16309–16321.
- [32] J. Zhang, J. Shao, J. Chen, et al., PFNet: an unsupervised deep network for polarization image fusion, *Opt. Lett.* 45 (6) (2020) 1507–1510.
- [33] P. Qi, X. Li, Y. Han, et al., U2R-pGAN: Unpaired underwater-image recovery with polarimetric generative adversarial network, *Opt. Lasers Eng.* 157 (2022) 107112.
- [34] D. Li, B. Lin, X. Wang, et al., High-Performance Polarization Remote Sensing with the Modified U-Net Based Deep-Learning Network, *IEEE Trans. Geosci. Remote Sens.* 60 (2022) 1–10.
- [35] B. Lin, X. Fan, Z. Guo, Self-attention module in a multi-scale improved U-net (SAM-MIU-net) motivating high-performance polarization scattering imaging, *Opt. Express* 31 (2) (2023) 3046–3058.
- [36] B. Lin, W. Chen, X. Fan, et al., Transformer-based improved U-net for high-performance underwater polarization imaging, *Opt. Laser Technol.* 181 (2025) 111664.
- [37] B. Lin, X. Fan, D. Li, et al., High-Performance Polarization Imaging Reconstruction in Scattering System under Natural Light Conditions with an Improved U-Net, *Photonics* 10 (2) (2023) 204.
- [38] B. Lin, X. Fan, P. Peng, et al., Dynamic polarization fusion network (DPFN) for imaging in different scattering systems, *Opt. Express* 32 (1) (2024) 511–525.
- [39] X. Fan, W. Chen, B. Lin, et al., Improved polarization scattering imaging using local-global context polarization feature learning framework, *Opt. Lasers Eng.* 178 (2024) 108194.
- [40] Ronneberger O, Fischer P, Brox T, U-net: Convolutional networks for biomedical image segmentation, International Conference on Medical image computing and computer-assisted intervention, Springer2015, pp. 234–41.
- [41] J.C. Ramella-Roman, S.A. Prahl, S.L. Jacques, Three Monte Carlo programs of polarized light transport into scattering media: part I, *Opt. Express* 13 (12) (2005) 4420–4438.
- [42] W. Zhang, L. Zhou, P. Zhuang, et al., Underwater image enhancement via weighted wavelet visual perception fusion, *IEEE Trans. Circuits Syst. Video Technol.*, 2023.
- [43] C. Li, S. Anwar, F. Porikli, Underwater scene prior inspired deep underwater image and video enhancement, *Pattern Recognit.* 98 (2020) 107038.
- [44] Zhang D, Zhou J, Zhang W, et al. Synergistic Multiscale Detail Refinement via Intrinsic Supervision for Underwater Image Enhancement. arXiv preprint arXiv: 2308.11932 2023.
- [45] T. Hospedales, A. Antoniou, P. Micaelli, et al., Meta-learning in neural networks: A survey, *IEEE Trans. Pattern Anal. Mach. Intell.* 44 (9) (2021) 5149–5169.
- [46] D. Wang, F. He, Y. Yu, et al., Meta-learning for T cell receptor binding specificity and beyond, *Nat. Mach. Intell.* 5 (4) (2023) 337–339.
- [47] J. Dai, H. Qi, Y. Xiong, et al., Deformable convolutional networks, *Proc. IEEE Int. Conf. Comput. vis.* (2017) 764–773.
- [48] J. Feng, W. Zhang, Z. Li, et al., Deep-learning based image reconstruction for MRI-guided near-infrared spectral tomography, *Optica* 9 (3) (2022) 264–327.
- [49] B. Bai, Y. Li, Y. Luo, et al., All-optical image classification through unknown random diffusers using a single-pixel diffractive network, *Light Sci. Appl.* 12 (1) (2023) 69.
- [50] S. Luo, Y. Li, P. Gao, et al., Meta-seg: A survey of meta-learning for image segmentation, *Pattern Recognit.* 108586 (2022).
- [51] A. Paszke, S. Gross, F. Massa, et al., PyTorch: An imperative style, high-performance deep learning library, *Adv. Neural Inf. Proces. Syst.* 32 (2019).
- [52] S. Van der Walt, J.L. Schönberger, J. Nunez-Iglesias, et al., scikit-image: image processing in Python, *PeerJ* 2 (2014) e453.
- [53] M. Dubreuil, P. Delrot, I. Leonard, et al., Exploring underwater target detection by imaging polarimetry and correlation techniques, *Appl. Opt.* 52 (5) (2013) 997–1005.
- [54] P.L. Drews, E.R. Nascimento, S.S. Botelho, et al., Underwater depth estimation and image restoration based on single images, *IEEE Comput. Graphics Appl.* 36 (2) (2016) 24–35.
- [55] Dong H, Pan J, Xiang L, et al., Multi-scale boosted dehazing network with dense feature fusion, Proceedings of the IEEE/CVF conference on computer vision and pattern recognition2020, pp. 2157–67.
- [56] H. Ding, M. Ding, T. Lv, et al., Polarimetric Observable based Optical Remote Sensing Systems for Heterogeneous Layered Scattering Environments, *Opt. Lasers Eng.* 189 (2025) 108916.
- [57] D. Li, I. Montes, M. Canabal-Carbia, et al., Enhanced characterization of depolarizing samples using indices of polarization purity and polarization–reflection–transformation spaces, *Adv. Photonics Nexus* 4 (1) (2025) 016009–20109.